ACS Chemical Neuroscience

pubs.acs.org/chemneuro Research Article

Molecular Simulations Reveal Distinct Energetic and Kinetic Binding Properties of [^{18}F]PI-2620 on Tau Filaments from 3R/4R and 4R Tauopathies

Georg Künze,* Richy Kümpfel, Michael Rullmann, Henryk Barthel, Matthias Brendel, Marianne Patt, and Osama Sabri*

Cite This: *ACS Chem. Neurosci.* 2022, 13, 2222−2234 Read Online

ACCESS | Metrics & More | Article Recommendations | Supporting Information

ABSTRACT: Tauopathies are a class of neurodegenerative disorders characterized by the accumulation of tau protein filaments in the brain. On the basis of isoforms with three or four microtubule-binding repeats (3R or 4R) that constitute tau filaments, tauopathies can be divided into 3R, 4R, and 3R/4R tauopathies. [^{18}F]PI-2620 is a tau-positron emission tomography (PET) tracer that detects tau filaments in the 3R/4R tauopathy Alzheimer's disease (AD) and the 4R tauopathies corticobasal degeneration (CBD) and progressive supranuclear palsy (PSP) with differential binding characteristics. A multiscale simulation workflow, including molecular docking, molecular dynamics simulation, metadynamics, and Brownian dynamics, was applied to uncover the molecular basis for the different binding properties of [^{18}F]PI-2620 in these tauopathies. The energetically best binding sites of [^{18}F]PI-2620 in the AD-tau filament are located in the C-shaped groove of the filament core structure that is accessible to the outside. The most favorable binding sites in CBD-tau and PSP-tau filaments are localized to cavities in the inner filament core. Sites on the outer surface have higher binding free energies, and interaction of [^{18}F]PI-2620 at these sites was short-lived in the molecular dynamics simulations. Computationally predicted associated rates of [^{18}F]PI-2620 with the groove sites in the AD-tau filament were higher than association rates with the cavity sites in the CBD- and PSP-tau filaments. The results indicate that tau filaments in AD combine favorable energetic and kinetic properties with regard to tracer binding, while the binding of [^{18}F]PI-2620 to filaments in CBD and PSP is kinetically restricted. Our findings reveal that distinct structural, energetic, and kinetic properties of tau filaments from AD, CBD, and PSP govern their interaction with PET tracers, which highlights the possibility to achieve tau isoform specificity in future tracer developments.

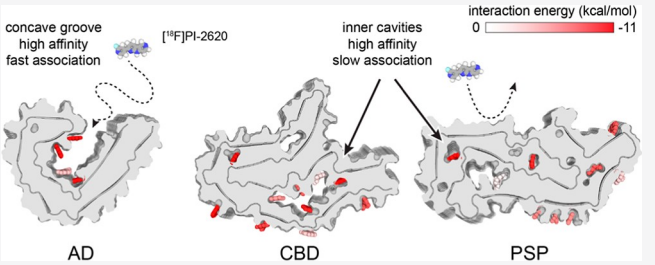

KEYWORDS: *tau, PET tracer, tauopathies, protein filaments, molecular docking, molecular dynamics simulation, PI-2620*

INTRODUCTION

Tauopathies are a class of neurodegenerative diseases characterized by the abnormal deposition of tau proteins in the human brain. Alzheimer's disease (AD) is the most common tauopathy and the most prevalent cause of dementia.[1] The care of AD patients leads to significant health care costs, making research to contribute to early diagnosis and therapy of primary importance.[1] Tau deposits are also causative of other neurodegenerative diseases such as progressive supranuclear palsy (PSP), corticobasal degeneration (CBD), chronic traumatic encephalopathy (CTE), and Pick's disease (PiD).[2−4] PSP is the most common tauopathy after AD.[5]

Tau has a well-established role as a microtubule-binding protein.[6] Hyperphosphorylation of tau leads to its aggregation and the formation of filaments, causing a breakdown of microtubules and malfunction of neurons.[7] Negative-stain electron microscopy (EM) shows that the filaments consist of a rigid core with a typical cross-β structure, whereas the amino- and carboxy-terminal regions of tau filaments are disordered and project away from the core to form a fuzzy coat.[8]

Six tau isoforms ranging in size from 352 to 441 amino acids are expressed in the human brain.[9,10] They can be distinguished by the occurrence of three (3R) or four (4R) microtubule-binding repeats. It has been found that different tauopathies are dominated by specific tau isoforms.[11] In AD and CTE, tau filaments consist of both 3R and 4R isoforms. In PSP and CBD, only 4R tau isoforms are found, whereas in PiD, only filaments made of 3R tau are present. Moreover, tauopathies can be distinguished by the occurrence of distinct tau filament

Received: May 13, 2022
Accepted: June 15, 2022
Published: June 28, 2022

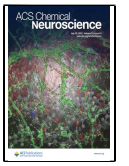

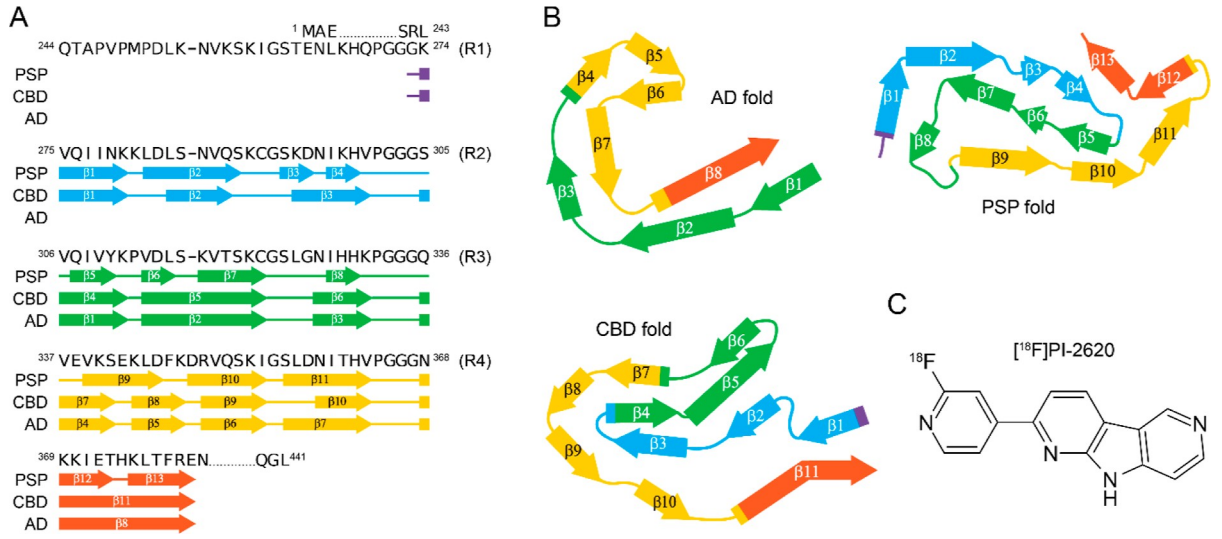

Figure 1. Structures of tau filaments and of [^{18}F]PI-2620. (A) Diagram showing the amino acid sequence of microtubule-binding repeats (R1−R4) of tau and of the region after R4. β-Strands found in the core structures of tau filaments from AD, CBD, and PSP are marked with arrows and labeled consecutively. β-Strands belonging to R1−R4 and the region after R4 are colored purple, blue, green, yellow, and red, respectively. (B) Schematic diagrams of the tau filament core structures seen in AD ("AD fold"), CBD ("CBD fold"), and PSP ("PSP fold"). β-Strands are marked with arrows. The same color and labeling schemes as in (A) are used. (C) Chemical structure of the tau-PET tracer [^{18}F]PI-2620.

morphologies, which could be revealed in recent cryo-EM studies.[12−17] This observation has led to the suggestion of a structure-based classification of human tauopathies.[17]

The three-dimensional structure of tau filaments from individuals with AD (referred to as AD-tau) was determined in 2017.[12] The core of the AD-tau filament structure consists of repeats R3 and R4 and 10 residues of the C-terminal extension after R4 (Figure 1A), forming 8 β-sheets that fold into a double-layered, C-shaped structure (Figure 1B). In 2020, Zhang et al. reported the structure of tau filaments obtained from cases with CBD (referred to as CBD-tau).[16] The CBD-tau core comprises the last residues of R1, all of R2 to R4, and 12 residues of the C-terminal extension after R4 (Figure 1A). The core of CBD-tau filaments is composed of 11 β-sheets that together form a 4-layered structure (Figure 1B). CBD-tau filaments contain a large internal cavity, which is lined by polar and positively charged amino acids and which enclosed an additional density in the experimental cryo-EM map.[16] It is possible that this extra density corresponds to polyanionic molecules that were incorporated in the CBD-tau filament during filament assembly. Structure determination of the tau filaments from human subjects with PSP (termed PSP-tau) revealed yet another filament structure.[17] The core of the PSP-tau filament structure contains the last 3 residues of R1, all of R2 to R4, and 13 residues after R4 (Figure 1A). These segments form 13 β-sheets that together fold into a 3-layered, meandered structure (Figure 1B). Similar to the CBD-tau filament, the structure of the PSP-tau filament contains internal cavities that are filled by extra densities in the experimental cryo-EM map. In addition to the tau filaments from AD, CBD, and PSP, the structures of tau filaments involved in other tauopathies (e.g., CTE,[15] PiD[14]) were also determined. This revealed an impressive diversity of tau filament folds, hinting at the possibility of developing structure-based strategies for the selective detection of specific tauopathies.

A major goal in the management of tau-related neurological disorders is the quantification of pathological tau levels because progression of tau pathology is closely correlated with increased neurodegeneration and cognitive impairment in AD and other tauopathies. Noninvasive imaging of tau deposits by positron emission tomography (PET) has become an indispensable tool allowing for differential dementia diagnosis and for monitoring of disease progression and drug effects. Small-molecule PET tracers for imaging of tau lesions in the brain have been developed and also tested in patient cohorts.[18−20] In 2020, [^{18}F]flortaucipir ([^{18}F]AV-1451), one of the first-generation tau tracers, has received approval by the US Food and Drug Administration (FDA) for the use in patients being evaluated for AD.[21] However, several first-generation tau-PET tracers [e.g., [^{11}C]PBB3,[22] [^{18}F]THK5351,[23] and [^{18}F]AV-1451 (also termed [^{18}F]T807)[24]] show limitations, such as off-target binding to enzymes and other proteins of the central nervous system,[25] which limits the use of these tracers in a clinical setting. Improvements in binding affinity and selectivity have been achieved by the development of second-generation tau tracers. [^{18}F]PI-2620 (Figure 1C) is a tracer that shows high affinity for aggregated tau in the AD brain homogenate and preparations of tau paired helical filaments.[26] [^{18}F]PI-2620 binds both 3R and 4R tau isoforms and demonstrates high selectivity over β-amyloid and α-synuclein.[26] In addition, [^{18}F]PI-2620 shows excellent blood−brain barrier permeability and favorable kinetic properties, which makes it a promising tau-PET tracer.[27]

The focus of tracer development has been on targeting AD, and only a few tracers have been evaluated for their use in other tauopathies. Consequently, little is understood about the factors contributing to the distinct binding properties of PET tracers toward tau filaments in non-AD tauopathies. Although for certain scenarios, it may be desirable to have a tracer that can be used for imaging multiple tauopathies with 3R and/or 4R tau isoforms, there is the alternative concept of developing isoform-specific tau-PET tracers. Some promising results for imaging of tau filaments in PSP have been achieved with [^{18}F]PI-2620.[28] Another study by our group[29] showed that there are significant binding kinetics differences for [^{18}F]PI-2620 in tau-positive cortical brain regions of patients with the 3R/4R tauopathy AD versus patients with the 4R tauopathies PSP or CBD. Higher clearance of [^{18}F]PI-2620 in cases with the 4R tauopathies

https://doi.org/10.1021/acschemneuro.2c00291
ACS Chem. Neurosci. 2022, 13, 2222−2234

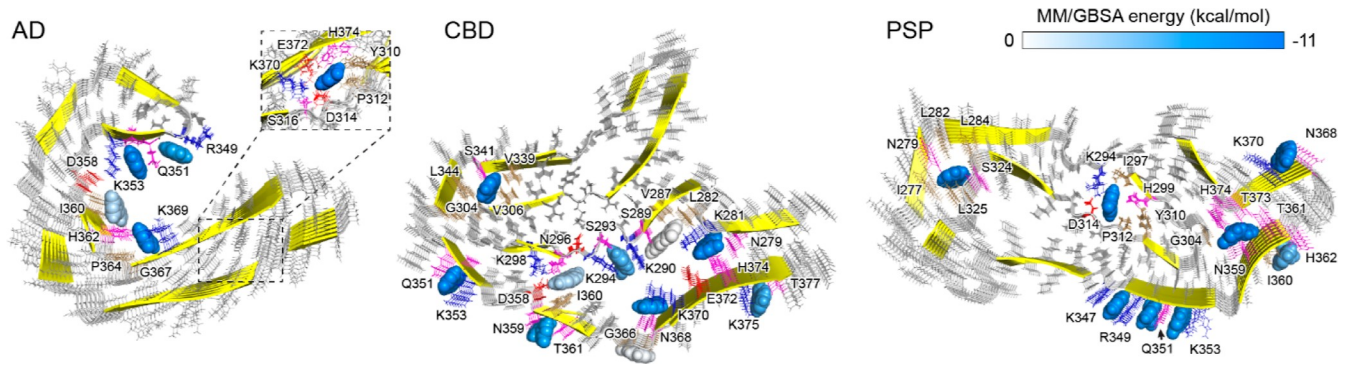

Figure 2. Putative binding sites of [^{18}F]PI-2620 in tau filaments predicted by docking and MD simulation. [^{18}F]PI-2620 binding poses in the core structures of AD-tau, CBD-tau, and PSP-tau filaments. β-Sheets are colored yellow, amino acid side chains are shown as sticks, and [^{18}F]PI-2620 molecules are depicted with spheres. Residues interacting with [^{18}F]PI-2620 are colored by their chemical properties: red—Glu and Asp (negatively charged); blue—Lys and Arg (positively charged); magenta—Gln, Asn, His, Ser, and Thr (polar); and sand—Ala, Val, Leu, Ile, Gly, Pro, Cys, Phe, Tyr, and Trp (apolar). [^{18}F]PI-2620 molecules are colored according to their binding free energies (Table 1). For the AD-tau structure (left), the figure inset shows the location of an additional cavity site that appeared when running MD simulations (see also Figure 6). All docking poses obtained for [^{18}F]PI-2620 on AD-tau, CBD-tau, and PSP-tau filaments are shown in Supporting Information Figures S1−S3, respectively, and all binding energies and RMSD values are listed in Supporting Information Tables S1−S3, respectively.

indicated less stable tracer binding compared to AD cases. This is in line with the in vitro-measured lower binding affinity of [^{18}F]PI-2620 to 4R tau (pIC_{50} 7.7 ± 0.1 for PSP brain tissue) compared to 3R/4R tau (pIC_{50} 8.5 ± 0.1 for AD brain tissue).[26] This information could be helpful for the differential diagnosis of 3R/4R and 4R tauopathies. Recently, a novel PET tracer, [^{18}F]APN-1607, with high binding affinity for tau deposits in AD and PSP was developed.[30] Initial results suggest that [^{18}F]APN-1607 is a potent tracer for the diagnosis and disease severity assessment in patients with PSP.[31] Despite the favorable properties of [^{18}F]PI-2620 and other second-generation tau-PET tracers, little is known about their molecular binding mechanisms. Furthermore, the molecular basis for the different binding characteristics of 3R/4R tauopathies versus 4R tauopathies is currently not understood. To explain the differential binding profiles of tau-PET tracers in different tauopathies, computational modeling methods provide an essential tool to study the interaction mode of tau filaments with PET tracers at the atomic level.

Murugan et al.[32] used molecular docking to predict putative binding sites of [^{18}F]PBB3, [^{18}F]TK5351, [^{18}F]AV-1451, and [^{18}F]MK-6240 in AD-tau filaments. Kuang et al.[33] investigated the interaction of [^{18}F]PI-2620 with the AD-tau filament structure using computational docking, molecular dynamics (MD) simulation, and free energy calculations. These studies revealed multiple binding sites on the filament surface with overlapping locations between tracers but differences in the binding energies. The energetically most favorable binding sites were found on the concave side of the C-shaped tau filament structure. Zhou et al.[34] compared the binding site locations and energies of [^{18}F]PI-2620, [^{18}F]MK-6240, [^{18}F]CBD-2115, and [^{18}F]APN-1607 in AD-tau filaments with those identified in CBD-tau filaments. Although tracers showed some binding energy differences, none of the tracers was fully selective for either AD-tau or CBD-tau filaments. Some selectivity was found for [^{18}F]AV-1451 in computational simulations using the AD-tau and PiD-tau filament structures.[35] Murugan et al. carried out MD simulations in an organic solvent (benzene), which induced an opening of putative cryptic sites in the AD-tau filament structure. These sites are closed in the cryo-EM-determined structure but become accessible to [^{18}F]AV-1451 after weakening of protein hydrophobic interactions. The binding energy differences between these cryptic sites in the AD-tau filament structure compared to sites in the PiD-tau filament structure were in line with the order of experimentally observed binding affinities.

The aim of the current study was to identify the molecular mechanisms underlying the different binding characteristics of [^{18}F]PI-2620 in 3R/4R versus 4R tauopathies. Using a multiscale simulation workflow, including molecular docking, MD simulations, molecular mechanics / generalized Born surface area (MM/GBSA) calculations, and metadynamics simulations, we identified the binding sites of [^{18}F]PI-2620 in the tau filament core structures from AD, CBD, and PSP and determined the tracer binding free energies and association rates. Our results indicate that tau filaments in AD and non-AD tauopathies differ in these molecular properties which emphasizes the possibility to achieve tau isoform specificity with certain PET tracers.

RESULTS AND DISCUSSION

[^{18}F]PI-2620 Exhibits Low-Energy Binding Sites in the C-Shaped Groove of the AD-Tau Filament. We used the cryo-EM structure of the AD-tau filament as the starting point for docking of [^{18}F]PI-2620. To consider all possible tracer binding sites, the AD-tau filament structure was fully surrounded by a grid of starting positions for ligand docking. The interaction of [^{18}F]PI-2620 with the filament structure was exhaustively probed by generating 50,000 docking models with the RosettaLigand docking program.[36,37] The most probable binding sites were identified by clustering of the best 20% docking poses with the lowest interface energies. Supporting Information Figure S1 displays representative docking poses of [^{18}F]PI-2620 for the largest clusters. Each docking model was further refined by running MD simulations of the tau-[^{18}F]PI-2620 complex in explicit water to assess the stability of tracer binding poses. MM/GBSA energy analysis was applied to compute the binding energy for each tracer binding site. Furthermore, to evaluate the stability of each binding pose, MD simulations were extended up to >500 ns, and the root-mean-square distance (RMSD) of each tracer molecule relative to its starting configuration was measured. At some sites, [^{18}F]PI-

https://doi.org/10.1021/acschemneuro.2c00291
ACS Chem. Neurosci. 2022, 13, 2222−2234

Table 1. MM/GBSA Energies and Locations of [^{18}F]PI-2620 Binding Sites in AD-Tau, CBD-Tau, and PSP-Tau Filaments

binding site residues	location		$\Delta G_{binding}$ [a]
	AD-tau		
H362, P364, G367, N368, K369	surface	β7, β8	−11.61 ± 0.26
I360, T361, H362	surface	β7	−2.67 ± 0.14
Q351, S352, K353	surface	β6	−10.16 ± 0.23
R349, V350, Q351	surface	β6	−10.08 ± 0.14
Y310, P312, V313, D314, S316, K370, E372	cavity	β1, β2, β8	−11.47 ± 0.22
	CBD-tau		
Q351, S352, K353	surface	β9	−10.82 ± 0.15
D358, N359, I360, T361	surface	β10	−7.37 ± 0.14
K375, L376, T377	surface	β11	−6.11 ± 0.15
N296, D358, I360, H362	cavity	β3, β10	−2.73 ± 0.21
K290, S293, K294	cavity	β2-β3 loop	−5.74 ± 0.22
N368, K369, K370	cavity	β11	−8.89 ± 0.17
N279, K280, K281, L282, H374	cavity	β1, β11	−12.31 ± 0.21
K281, L282, V287, S289	cavity	β2, β1-β2 loop	0.81 ± 0.14
G304, S305, V306, V339, K340, S341, L344	cavity	β4, β7, β8	−17.34 ± 0.16
	PSP-tau		
D345, K347, D348, R349	surface	β10	−9.18 ± 0.11
R349, V350, Q351	surface	β10	−8.69 ± 0.11
V350, Q351, S352, K353	surface	β10	−8.56 ± 0.14
I360, T361, H362	surface	β11	−5.23 ± 0.08
N368, K369, K370	surface	β12	−10.69 ± 0.11
I277, N279, L282, L284, G323, S324, L325	cavity	β1, β2, β7-β8 loop	−19.44 ± 0.14
K294, I297, H299, Y310, P312, V313, D314	cavity	β3, β4, β6	−13.51 ± 0.11
N359, I360, T361, T373, H374	cavity	β4-β5 loop, β11, β12	−11.21 ± 0.26

[a]Energy is given as mean ± SEM in units kcal/mol.

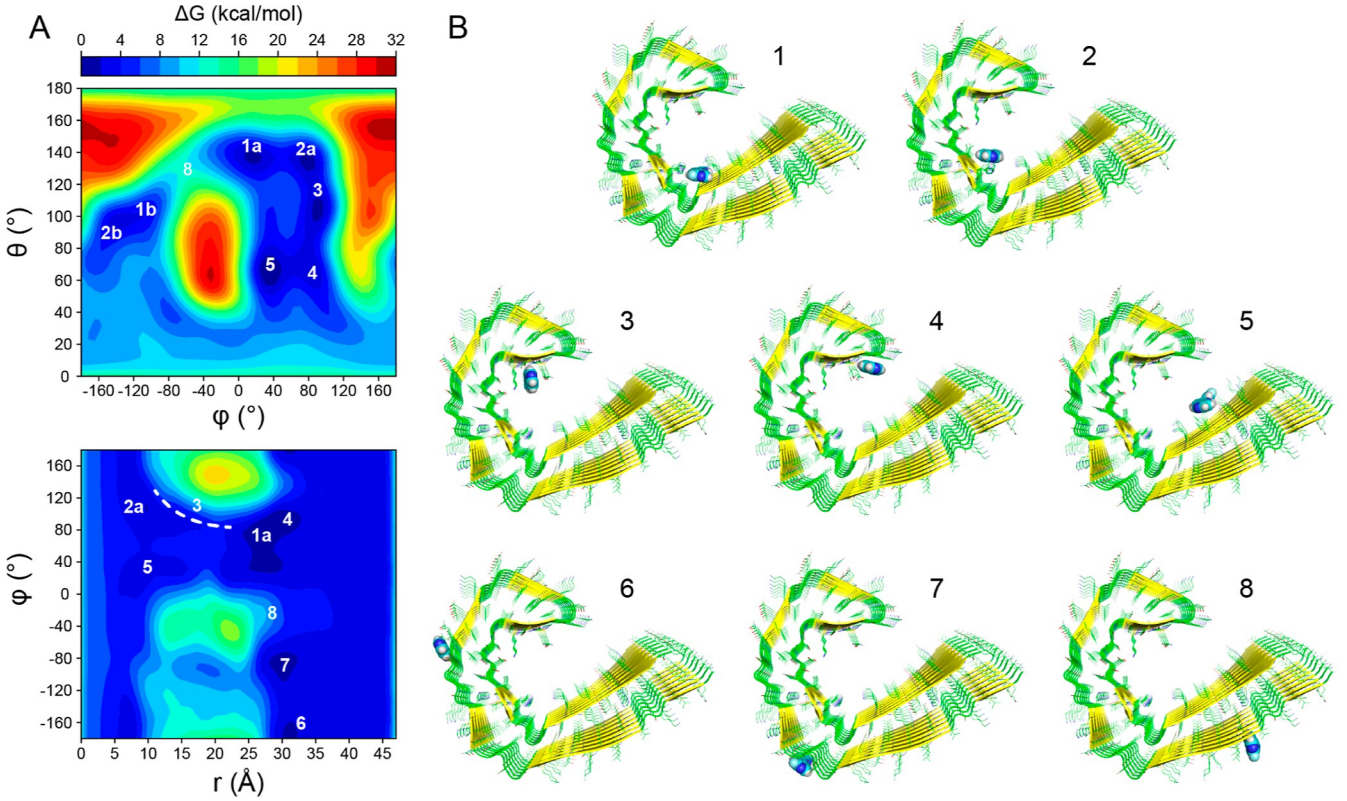

Figure 3. Free energy surface for the interaction of [^{18}F]PI-2620 with an AD-tau filament obtained by a metadynamics simulation. (A) 2D free energy maps in the space spanned by the CVs used in the metadynamics simulation. The location of energy minima is labeled. (B) Depiction of the binding poses of [^{18}F]PI-2620 which correspond to the energy minima in (A).

https://doi.org/10.1021/acschemneuro.2c00291
ACS Chem. Neurosci. 2022, 13, 2222−2234

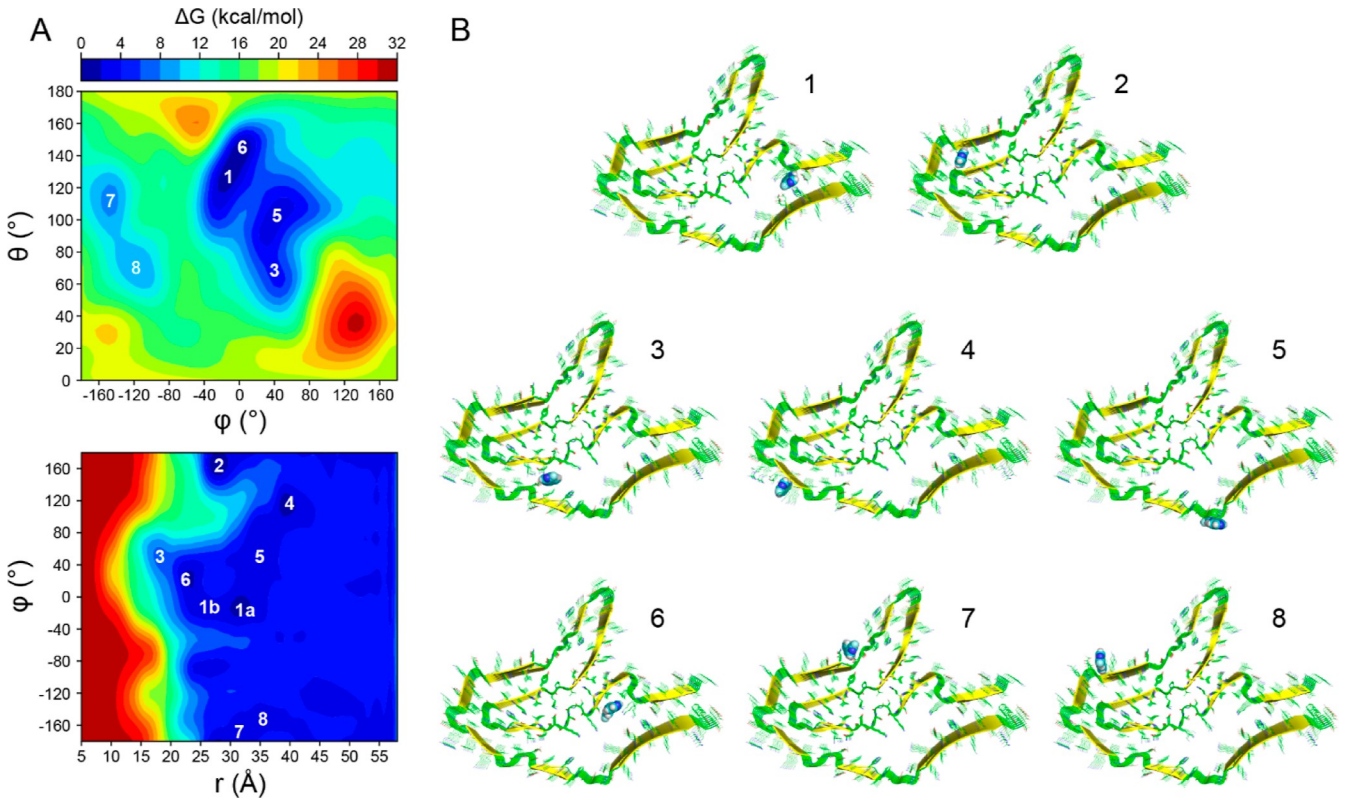

Figure 4. Free energy surface for the interaction of [^{18}F]PI-2620 with a CBD-tau filament obtained by a metadynamics simulation. (A) 2D free energy maps in the space spanned by the CVs used in the metadynamics simulation. (B) Depiction of the binding poses of [^{18}F]PI-2620 which correspond to the energy minima in (A).

2620 molecules were observed to quickly dissociate from the filament surface, while at other sites, tracers remained stably bound over the entire length of the MD simulation. These binding sites where [^{18}F]PI-2620 molecules remained bound in the MD simulation are shown in Figure 2 on the left-hand side. The MM/GBSA energies and interacting protein residues for these binding sites are summarized in Table 1. The MM/GBSA energies for all [^{18}F]PI-2620 docking poses in the AD-tau filament are listed in Supporting Information Table S1. Most important amino acid residues that interact with [^{18}F]PI-2620 were identified by calculating the per-residue contributions to the total binding free energy. As can be seen in Figure 2, the most stable binding poses of [^{18}F]PI-2620 on the surface of the AD-tau filament are formed in the central groove of the C-shaped filament structure. The lowest-energy binding sites exist at the β6 strand, where tracer molecules intercalate between the side chains of R349, Q351, and K353. Another low-energy binding site is formed by residues at the tip of β7, the β7−β8 connecting loop, and the start of β8. MM/GBSA energy analysis showed that residues H362, P364, G366, G367, N368, and K369 interact most strongly with the tracer at this site. Another low-energy binding site between two β-sheet layers appeared when running MD simulations. This binding site is described in more detail below.

Exhaustive Sampling of [^{18}F]PI-2620 Binding Sites in the AD-Tau Filament by Metadynamics Simulation. In order to check if there could be additional tracer binding sites in the AD-tau filament which were not detected by the back-to-back docking and MD approach, we used a complementary method and performed well-tempered multiple walker metadynamics simulations of [^{18}F]PI-2620 with tau filaments. This offered a way to enhance the conformational sampling and construct the free energy map for the tau-[^{18}F]PI-2620 interaction. As collective variables in the metadynamics simulation, we used the three spherical coordinates (r, θ, and φ) that describe the position of the tracer molecule relative to the center of mass of the filament. The geometric definition of the collective variables is depicted in Supporting Information Figure S4. Further details on the setup and analysis of the metadynamics simulation and reweighting procedure are given in Methods. Figure 3A shows the free energy map in the space spanned by the collective variables, and Figure 3B shows molecular representations of the binding modes corresponding to the lowest free energy minima. Consistent with the results obtained by docking and MM/GBSA analysis, the lowest-energy binding sites of [^{18}F]PI-2620 are located in the C-shaped groove of the filament. Three additional low-energy binding sites are found on the outer convex surface at β1−β2, β2−β3, and β3−β4 connecting loops. The binding poses on the outer convex surface were also observed in the docking experiments; however, [^{18}F]PI-2620 molecules dissociated rapidly from these sites when running MD as evidenced by the high RMSD values (Table S1). Overall, the metadynamics simulation identified the same binding sites as observed in docking and MD and confirmed that the energetically most favorable tracer binding sites in AD-tau filaments exist in the C-shaped groove.

Spacious Cavity in the CBD-Tau Filament Offers Multiple Binding Sites for [^{18}F]PI-2620 in Addition to Sites on the Outer Surface. Next, we investigated the interaction of [^{18}F]PI-2620 with the tau filament from CBD using the same workflow of ligand docking, MD simulation, and MM/GBSA energy analysis. Supporting Information Figure S2

https://doi.org/10.1021/acschemneuro.2c00291
ACS Chem. Neurosci. 2022, 13, 2222−2234

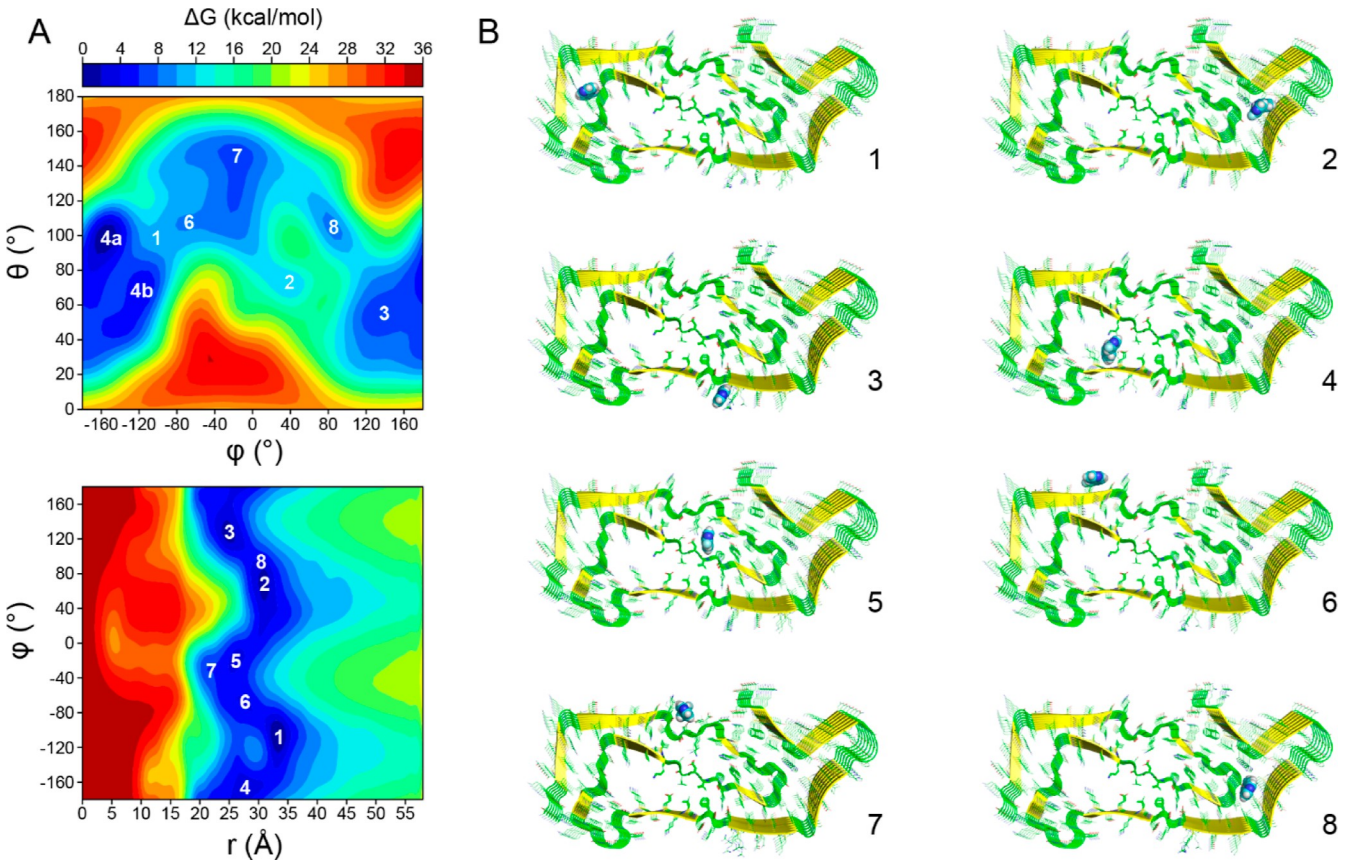

Figure 5. Free energy surface for the interaction of [^{18}F]PI-2620 with a PSP-tau filament obtained by a metadynamics simulation. (A) 2D free energy maps in the space spanned by the CVs used in the metadynamics simulation. (B) Depiction of the binding poses of [^{18}F]PI-2620 which correspond to the energy minima in (A).

displays binding poses of [^{18}F]PI-2620 in the CBD-tau filament predicted by docking and clustering of docked poses. Figure 2 shows the binding modes of [^{18}F]PI-2620 which were deemed most stable because the position of [^{18}F]PI-2620 at these sites changed marginally in the 500 ns-long MD simulation. The MM/GBSA binding energies computed for these sites are summarized in Table 1, and the MM/GBSA energies determined for all docked poses are listed in Supporting Information Table S2. As can be seen in Figure 2, most of the stable [^{18}F]PI-2620 interaction sites are located within an inner cavity formed by β2 and β3 strands on one side and β10 and β11 strands on the other side. In addition, there are some low-energy surface sites on β9, β10, and β11. The lowest-energy binding site, however, is formed by a narrow cavity between β4, β7, and β8 strands. Per-residue breakdown analysis of the MM/GBSA energies showed that more than 30 mostly hydrophobic residues interact with [^{18}F]PI-2620 at this site which explains its exceptionally favorable binding energy of −17.34 kcal/mol. The next most favorable binding site has a computed binding energy of −12.31 kcal/mol for [^{18}F]PI-2620 and is formed by the sidechains of residues N279, K281, and H374 (Figure 2, Table 1).

We complemented the docking, MD, and MM/GBSA analyses with metadynamics simulations of the CBD-tau-[^{18}F]PI-2620 system using again the three spherical coordinates of the tracer as collective variables. The resulting free energy maps are displayed in Figure 4A, and molecular binding model representations of the corresponding energy minima are shown in Figure 4B. The two lowest-energy minima identified in the metadynamics simulation correspond to tracer binding at the two cavity sites mentioned above. The other energy minima represent interactions of [^{18}F]PI-2620 with residues either in the inner cavity or on the outer surface of the CBD-tau filament and match sites identified by docking and MM/GBSA analysis. In conclusion, the metadynamics simulation confirmed the docking and MD results and highlighted the importance of two cavity binding sites in the CBD-tau filament—one surrounded by mostly hydrophobic residues in β4, β7, and β8 strands and another formed by the long aliphatic side chains of polar residues at the interface between β1 and β11 strands.

Our data on the CBD-tau filament are in line with results by Zhou et al.[34] who applied a different metadynamics protocol. The authors discovered three energetically preferred cavity sites in the CBD-tau filament, one at β1 and β11 sheets, a second at β3 and β10 sheets, and a third at β4, β7, and β8 sheets, which agrees well with our findings. Binding on the outer surface was overall weak, but interaction of [^{18}F]PI-2620 with the outward curved side (β9, β10, and β11 sheets) was slightly stronger than with the inward curved side (β6, β7, and β8 sheets) of the filament, which is consistent with our simulation data on the CBD-tau filament (compare with Figure 2).

[^{18}F]PI-2620 Exhibits Multiple Low-Energy Cavity Binding Sites in the PSP-Tau Filament. As noted, CBD and PSP are both 4R tauopathies but present filaments with different morphologies. Most notably, filaments in CBD have a four-layered β-structure core, whereas the PSP fold comprises only three β-structure layers. Because these different folds lead to differences at the residue level, we sought to investigate the

https://doi.org/10.1021/acschemneuro.2c00291
ACS Chem. Neurosci. 2022, 13, 2222−2234

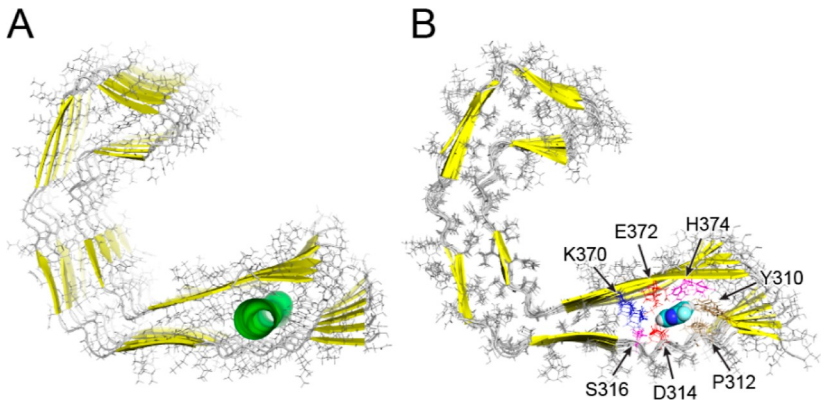

Figure 6. MD simulations reveal an aqueous pore in AD-tau filaments which is accessible to [^{18}F]PI-2620. (A) MD snapshot of an AD-tau protofilament. A solvent-filled pore (represented by the green surface) is present between two β-sheets. (B) MD snapshot of an AD-tau protofilament with a [^{18}F]PI-2620 molecule bound inside the pore. Residues that interact with [^{18}F]PI-2620 are displayed as colored sticks and labeled.

interactions of [^{18}F]PI-2620 with filaments from PSP. Figure 2 shows the most favorable binding sites of [^{18}F]PI-2620 in the PSP-tau filament obtained by docking and validation of docked poses by running MD simulations. MM/GBSA binding energies for these sites are listed in Table 1. All docked poses of [^{18}F]PI-2620 and the corresponding MM/GBSA energies are presented in Figure S3 and Table S3, respectively. Three binding sites are at the surface of β10. Additional surface sites exist at β11 and β12 sheets. Notably, up to four cavity binding sites are observed in the PSP-tau filament; three of them ranked at the top in terms of MM/GBSA energies. Two of the three lowest-energy binding sites are sandwiched between R2 and R3 repeats. Residues I277, N279, L282, and L284 in R2 and S324 and L325 in R3 contribute to the first mostly hydrophobic cavity site, and K294, I297, H299, Y310, P312, and D314 form the second cavity site. A third low-energy cavity site, which has mostly a polar character, is bordered by G304 in R2, N359 and T361 in R4, and T373 and H374 in the C-terminal domain. Metadynamics simulations of the [^{18}F]PI-2620-PSP-tau filament system were conducted using the same protocol as for AD-tau and CBD-tau filaments. Figure 5A shows the free energy maps for the interaction of [^{18}F]PI-2620 with the PSP-tau filament structure, and Figure 5B displays representative conformations from the MD simulation corresponding to the free energy minima. The lowest-energy minima identified in the energy maps include the binding poses at the three cavity sites described above, which is in very good agreement with the results obtained by docking and running regular MD simulation.

Cryptic Binding Site of [^{18}F]PI-2620 Revealed in the AD-Tau Filament Structure. Because ligand docking was performed with the cryo-EM structure of AD-tau filaments, which has a rigid, densely packed protein core, only binding sites on the filament surface were identified in docking and subsequently analyzed by MD. However, MD simulations revealed flexibility of filaments and a frequent bending of β-sheet structures. Strikingly, we observed in MD simulations of free and [^{18}F]PI-2620-bound AD-tau filaments that the residue packing between β1 and β2 strands on one side and the β4 strand on the opposite side of the filament became weaker, leading to the appearance of gaps and finally the formation of a water-filled pore. As can be seen in Figure 6A, this pore spans along the entire filament and is wide enough to accommodate a [^{18}F]PI-2620 molecule. Formation of this pore is likely a consequence of the charged and polar nature of amino acids that are sandwiched between the two β-sheet layers of the filament. Residues D314, S316, K370, E372, and H372 are located inside the filament core and favorably interact with water molecules in the MD simulations, leading to a permeation of water into the filament and creation of a tunnel that is large enough for small ligands. In contrast, the rest of the filament core contains almost exclusively hydrophobic amino acids that establish a tight packing of opposite β-sheets and prevent water from entering in the filament structure. To study whether the pore found in the AD-tau filament structure can represent a potential tracer binding site, we next docked [^{18}F]PI-2620 into the pore and performed MD. Figure 6B shows a representative snapshot of [^{18}F]PI-2620 occupying the pore site. The binding energy of [^{18}F]PI-2620 at the pore site (−11.47 kcal/mol; Table 1) is as low as for the most favorable surface site (−11.61 kcal/mol). These results support the possibility of cryptic sites in the AD-tau filament which could become accessible to PET tracers. These sites could be difficult to detect under the cryogenic conditions used in EM experiments but could exist when the filament is in a solvent at room temperature.

We could not observe the emergence of significant extra cavities in the CBD- and PSP-tau filament core structures in the MD simulations. However, we note that one cavity site formed by residues K294, I297, H299, Y310, P312, and D314 in the cryo-EM PSP-tau structure has a very similar shape and includes partly the same residues as the cryptic site in the AD-tau structure (see structural comparison in Figure 7). This supports the idea that the cryptic site in the AD-tau filament could represent a stable state. We note that Kuang et al. previously observed more than one cryptic binding site in the AD-tau filament when running MD simulations in an organic solvent.[33] One cryptic site found by Kuang is identical to the pore site shown in Figure 6A. The other cryptic sites reported by Kuang et al. were smaller, and we did not observe a spontaneous opening of them in the simulations. It must also be noted that the solvation of the filament structure in benzene, as used by Kuang et al., represents a rather harsh condition, and further investigations are needed to clarify if the cryptic sites predicted for the AD-tau filament can exist under physiological conditions.

[^{18}F]PI-2620 Binding Sites Agree with the Location of Nonproteinaceous Densities in Tau Cryo-EM Maps. Some experimental evidence on the location of tracer binding sites in tau filaments can be gained from the observation of non-proteinaceous electron densities in the experimental cryo-EM maps. In the maps determined for AD-tau,[12,38] CBD-tau,[16] and PSP-tau,[17] there are several smaller densities that are close to

https://doi.org/10.1021/acschemneuro.2c00291
ACS Chem. Neurosci. 2022, 13, 2222−2234

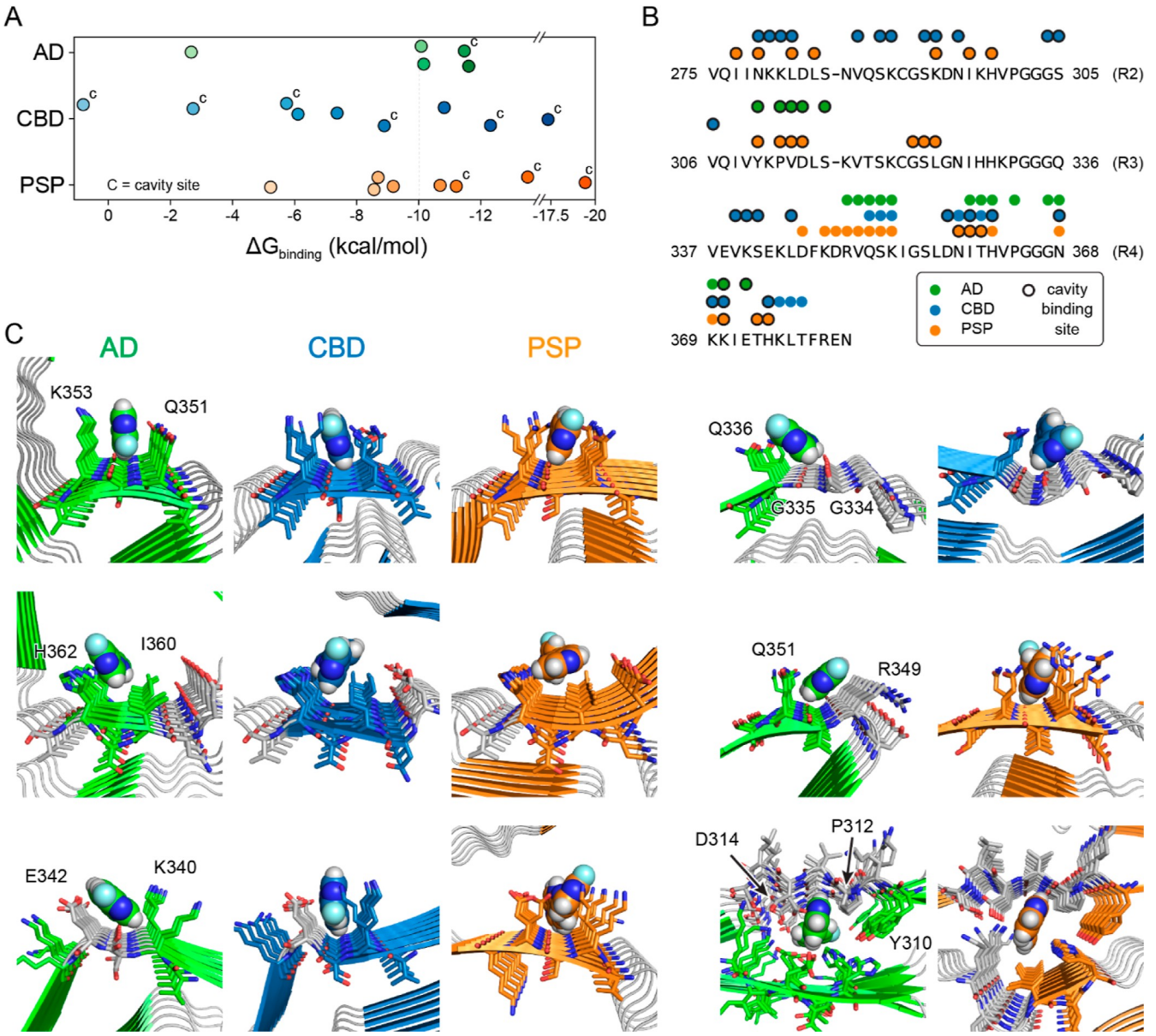

Figure 7. Comparison of the energies and locations of [^{18}F]PI-2620 binding sites in tau filaments from AD, CBD, and PSP. (A) MM/GBSA energies of the [^{18}F]PI-2620 binding poses displayed in Figures 2 and 6. Energy values for cavity sites are indicated with the label "C". (B) Location of [^{18}F]PI-2620 binding sites in the core structures of tau filaments from AD, CBD, and PSP is mapped as dots onto the tau amino acid sequence. Cavity sites are indicated by a black stroke. (C) Close-up views of [^{18}F]PI-2620 binding sites that are shared between AD-tau, CBD-tau, and PSP-tau filaments. Residues interacting with [^{18}F]PI-2620 in the structure models are indicated as sticks and labeled by their one-letter amino acid code and sequence number.

specific amino acid side chains in tau but not directly connected to the main density that corresponds to the tau polypeptide chain. These smaller densities likely correspond to ions, cofactors, or other small molecules that associate with the tau filament through electrostatic and/or hydrophobic interactions. Furthermore, Shi et al. obtained cryo-EM maps of AD-tau in the presence of [^{18}F]APN-1607 showing extra densities that could correspond to the tracer, even though the map resolution was not high enough to accurately position the tracer molecule in model building. Figure S5 compares the locations of these non-proteinaceous densities with the binding sites of [^{18}F]PI-2620 predicted by docking and MD simulation. Overall, there is an astonishingly good agreement between their locations. In the AD-tau map, there are three strong densities in the central groove at K353, Q351, and R349, which map to two low-energy binding sites of [^{18}F]PI-2620 and a weak density on the outer convex surface, which corresponds to a binding site with weaker interactions. In the CBD-tau map, one large density and three smaller densities are present in the inner filament core, in addition to two smaller densities on the outer surface. The smaller, confined densities in the inner core correspond to three cavity binding sites, and the outer densities at Q351 and N359 match two surface binding sites of [^{18}F]PI-2620. Finally, in the PSP-tau map, three densities in the inner core between β-sheet layers and three densities on the outer surface can be seen, which match three cavity sites and two surface binding sites predicted for [^{18}F]PI-2620. Overall, the results of this comparison strongly suggest that the [^{18}F]PI-2620 binding sites predicted in silico can also exist under physiological conditions.

https://doi.org/10.1021/acschemneuro.2c00291
ACS Chem. Neurosci. 2022, 13, 2222−2234

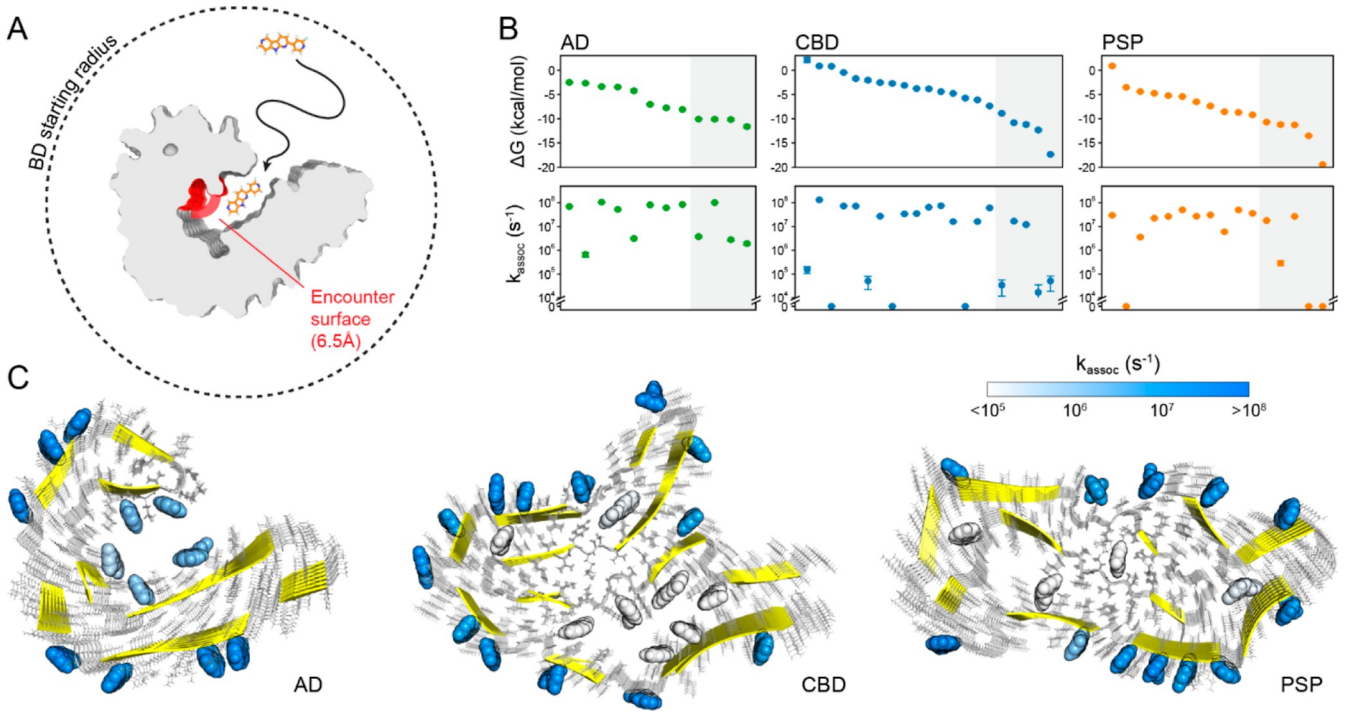

Figure 8. Association rates of [^{18}F]PI-2620 with tau filaments from AD, CBD, and PSP determined by BD simulations. (A) Schematic depiction of the simulation setup. The diffusion process of [^{18}F]PI-2620 from a sphere of radius 100 Å around the tau filament to the encounter surface at a distance of 6.5 Å from the protein binding site was treated with BD simulations. 10^6 single BD trajectories were calculated for each binding site and each tau filament structure. (B) Summary ΔG and k_{assoc} values of [^{18}F]PI-2620 determined for the binding poses in AD-, CBD-, and PSP-tau filaments shown in (C). The gray-shaded area indicates low-energy binding sites with $\Delta G < -10$ kcal/mol. For AD-tau, there are four low-energy sites on the surface. For both CBD-tau and PSP-tau, there are two surface and three cavity sites with low energy. (C) Docking poses of [^{18}F]PI-2620 in tau filaments from AD, CBD, and PSP colored by the corresponding association rate of [^{18}F]PI-2620 determined for the same docking site (white: $\leq 10^5$, blue: $\geq 10^8$).

Comparison of [^{18}F]PI-2620 Binding Sites in AD-Tau, CBD-Tau, and PSP-Tau Filaments. To learn more about the PET tracer binding specifics of filaments from AD, CBD, and PSP, we compared the locations and interaction energies of the [^{18}F]PI-2620 binding sites between the three filament forms. We found more tracer binding sites in the CBD- and PSP-tau filament than in the AD-tau filament; nine binding sites in the CBD-tau filament structure, eight in the PSP-tau filament structure, and five in the AD-tau filament structure were continuously occupied by a [^{18}F]PI-2620 molecule during docking and MD simulation. The difference in the number of binding sites is likely due to the different sizes of the filament core structures. As noted, the CBD and PSP filament core structures consist of repeats R2−R4 and part of the C-terminal domain, whereas the AD filament structure comprises only repeats R3 and R4 and 12 residues after R4.

Despite their different sizes, the tau filament structures from AD, CBD, and PSP have a similar number of low-energy binding sites for [^{18}F]PI-2620: four (AD), three (CBD), and four (PSP) binding sites with MM/GBSA energies below −10 kcal/mol could be found (Figure 7A). Looking at Figure 7A, it can be seen that most of these low-energy sites are located in molecular cavities. When comparing the locations of tracer binding sites, we were surprised to find many overlapping sites. Figure 7B shows that binding sites with the same or similar locations in AD, CBD, and PSP filaments are most often located in R4, the C-terminal domain, and the first half of R3. Figure 7C displays these common sites in the three-dimensional structures of AD-, CBD-, and PSP-tau filaments side-by-side. It is evident that these common sites adopt similar local conformations, which we refer to as microdomains. It is possible that these microdomains provide common interaction platforms, leading to some similarities of tracer binding properties. At the same time, the different global folds of AD-, CBD-, and PSP-tau filament structures create specific binding sites in these three filament forms.

Differences were noticed especially in the positions of low-energy binding sites of [^{18}F]PI-2620. For AD-tau, we identified by docking four sites on the protein surface with $\Delta G \leq -10$ kcal/mol (Table S1), three of which are located in the C-shaped groove of the AD-tau filament structure (Figure 2, left image). At these sites and another fourth binding site in the groove, [^{18}F]PI-2620 was firmly bound over the entire length of the MD simulations. By contrast, for CBD-tau and PSP-tau, only two surface sites with $\Delta G \leq -10$ kcal/mol were identified in docking (Tables S2 and S3). For only one of these surface sites (at β9 in CBD-tau, at β12 in PSP-tau), the interactions with [^{18}F]PI-2620 persisted over the 500 ns-long MD simulation, while interactions at the other surface sites (at β2 + β5 in CBD tau, at β2 in PSP-tau) were short-lived, leading to a dissociation of [^{18}F]PI-2620. On the other hand, CBD-tau and PSP-tau filaments have more cavity binding sites than AD-tau filaments. The number of low-energy sites ($\Delta G \leq -10$ kcal/mol) that exist at cavities in the CBD-tau and PSP-tau filament was found to be two and three, respectively (see Table 1; middle and right image in Figure 2). This compares to one cavity binding site in the AD-tau filament, which appeared only after simulating the filament in an explicit water environment. The higher number of cavity sites in CBD-tau and PSP-tau could be due to the fact that their filament core structures consist of four or three β-sheet layers,

https://doi.org/10.1021/acschemneuro.2c00291
ACS Chem. Neurosci. 2022, 13, 2222−2234

which are stacked on top of each other, whereas the AD-tau core structure comprises only two layers. The winding of β-sheet layers occurs at flexible PGGG motifs or at glycine residues, creating open spaces in the tau filament structure in which tracer molecules can fit. Thus, the four- and three-layered CBD and PSP folds lead to multiple cavity binding sites in the filament core, while the two-layered AD fold creates a groove with multiple surface accessible sites.

Association Rates of [^{18}F]PI-2620 with Surface Sites in the Central Groove in the AD-Tau Filament Are Higher Than Those with Cavity Sites in CBD-Tau and PSP-Tau Filaments. Besides energetic effects, the different nature of tracer binding sites in AD-tau versus CBD-tau and PSP-tau filaments could also affect the binding kinetics of [^{18}F]PI-2620. To test this hypothesis, we calculated the association rate of [^{18}F]PI-2620 with each predicted binding site using Brownian dynamics (BD) simulations. Figure 8A shows the setup of the BD simulations. At the beginning of each trajectory, [^{18}F]PI-2620 was placed at a spherical shell with a radius of 100 Å from the center of mass of the filament. The number of trajectories in which [^{18}F]PI-2620 reached the encounter surface at 6.5 Å from the amino acids of a selected binding site, before it diffused to distances larger than 300 Å from the filament center, was counted. Figure 8B shows the [^{18}F]PI-2620 association rates (k_{assoc}) of every binding site obtained by docking in AD-tau, CBD-tau, and PSP-tau filaments. For comparison, the MM/GBSA interaction energies are shown next to the k_{assoc} values. Figure 8C indicates the k_{assoc} values of every binding site in the filament 3D structures using a color gradient from white to blue. [^{18}F]PI-2620 molecules at sites with low $k_{assoc} \leq 10^5$ s^{-1} are colored white, and [^{18}F]PI-2620 molecules at sites with high $k_{assoc} \geq 10^8$ s^{-1} are colored blue.

For sites on the outer surface of tau filaments, k_{assoc} values range from 10^7 to 10^8 s^{-1}. For binding sites in the C-shaped groove in the AD-tau filament, k_{assoc} values are about 10 times smaller and range from 10^6 to 10^7 s^{-1}. Strikingly, the cavity sites in CBD-tau and PSP-tau filaments have even smaller k_{assoc} values of $\leq 10^5$ s^{-1}. For some cavity sites, no association event was observed in 10^6 BD trajectories. Although CBD-tau and PSP-tau filaments have also two energetically favorable surface sites with a high k_{assoc} of 10^7 s^{-1}, only one of these sites was stable in the MD simulation. In contrast, the AD-tau filament showed four low-energy sites which were stable in MD and have high k_{assoc} values between 10^6 and 10^7 s^{-1}.

Mechanistic Working Model for the Binding Behavior Differences of AD- and Non-AD-Tau Filaments. Our results show that the [^{18}F]PI-2620 binding sites in the AD-, CBD-, and PSP-tau filaments have different location and accessibility. In the AD-tau filament, the binding sites with the best interaction energies are located in the central groove that is accessible to the outside. In the CBD-tau and PSP-tau filaments, the lowest-energy binding sites are localized to cavities in the inner core that is accessible only from the two ends of the filament. The computed association rates of [^{18}F]PI-2620 with the groove sites in the AD-tau filament are 1 to 2 orders of magnitude higher than the association rates with the cavity sites in the CBD- and PSP-tau filaments. At the same time, the association rates on the outer surface of all three filament structures are similarly high, but the interaction energies for these sites are rather weak. Consequently, we observed that binding poses on the outer surface were short-lived in the MD simulations and dissociated from the filament in less than 500 ns, suggesting that surface-bound tracer molecules could be washed out more easily than molecules bound at the groove and cavity sites.

We hypothesize that the following molecular mechanism could underlie the observed binding behavior differences of [^{18}F]PI-2620 in 3R/4R versus 4R tauopathies. In AD, tracer molecules are located into the central groove that is accessible from the outside but also protected from interactions with the bulk solvent, enabling a strong and persistent tracer binding. In CBD and PSP, intercalation of tracer molecules into the inner filament core is slow, and tracers accumulate on the outer surface, where they can be washed out more easily because binding is rather weak. This mechanism could explain why [^{18}F]PI-2620 binding in cases with the 4R tauopathy appeared less stable and why tracer clearance was higher compared to AD.[29] The differences in the microscopic binding behavior are likely a consequence of the specific 3D folds of the three tau filaments. As noted, the AD-tau filament contains in its core structure two β-sheet layers that are curved to create a central groove. The core of the CBD-tau and PSP-tau filament consists of four and three β-sheet layers, respectively, that stack on each other and turn their direction several times, which creates room for small cavities. The locations of the small cavity sites are distinct for each tau filament. Exploration of these cavity sites could therefore represent a possible strategy to create tracer selectivity.

CONCLUSIONS

Our results show that the AD-tau filaments combine favorable energetic and kinetic properties with regard to tracer binding, whereas the interactions of [^{18}F]PI-2620 with CBD- and PSP-tau filaments are kinetically hindered. The results also suggest possible directions that could be explored in the design of new tau-PET tracers. The targeting of cavity sites could be an option to achieve tracer selectivity because these sites show different microstructures across different filament forms. The amount of tracer binding could be regulated, for example, by tuning the charge or size of the tracer to strengthen interactions with one cavity site but prevent binding to another cavity site. Furthermore, tuning the charge of the tracer could be used to regulate its binding kinetics through long-range electrostatics with the filament surface. Consistent with this idea, Kroth et al. found that derivatives of [^{18}F]PI-2620 which were generated by shifting the N-atom positions in the tricyclic aromatic ring have a changed electrostatic potential distribution, which could explain their inferior tau binding affinity and selectivity compared to [^{18}F]PI-2620.[39] MD simulations can be used to confirm structure−activity hypotheses and suggest further tracer modifications.

METHODS

Structure Preparation. The structures of tau filaments from AD (PDB: 5O3L),[12] type I (PDB: 6TJO) and type II (PDB: 6TJX) CBD,[16] and PSP (PDB: 7P65)[17] were obtained from the Protein Data Bank (PDB). Missing atoms were added using Rosetta software (version 3.12),[40] and the structures were minimized using the Rosetta ref2015 energy function[41] with distance constraints applied to all protein Cα atoms. For ligand docking and running MD simulations of tau filaments with [^{18}F]PI-2620, tau filament structures were extended by additional monomers to make sure that filaments were long enough in the direction of the longitudinal axis to bind a fully extended tracer molecule. For docking and MD simulations of [^{18}F]PI-2620, tau filaments consisted of 7 monomers, and for BD simulations, tau filaments contained 13 monomers. The molecular structure of [^{18}F]PI-2620 was built using Avogadro (version 1.2)[42] and optimized with

https://doi.org/10.1021/acschemneuro.2c00291
ACS Chem. Neurosci. 2022, 13, 2222−2234

Gaussian 09 (Gaussian, Inc, Wallingford CT) on the B3LYP/6-31G** level of theory. Assignment of Amber atom types and calculation of restrained electrostatic potential charges were done using Antechamber.[43] Generation of Rosetta params files was done as described previously.[44] Conformers of [^{18}F]PI-2620 used for ligand docking were generated with the BCL::conformer generator method.[45]

Ligand Docking. Docking of [^{18}F]PI-2620 to tau filaments was carried out using RosettaLigand[36,37,46] through RosettaScripts.[47,48] Prior to docking, a three-dimensional grid of ligand starting positions with 5 Å spacing was generated around the filament structure and used as the input to RosettaLigand. Unless otherwise stated, the default parameters of the RosettaLigand docking protocol were used. The maximum allowed translation of the ligand from its starting position was 8 Å, and the size of the ligand scoring grid was set to 35 Å × 35 Å × 35 Å. In the low-resolution stage, 1000 Monte Carlo moves of the ligand with a maximum translation of 0.2 Å and a maximum rotation of 20° per step were performed. In the high-resolution stage, the *ligand.wts* scoring function was used, and six cycles of alternating protein sidechain and ligand conformer packing followed by a final minimization of the protein−ligand interface were performed. A total of 50,000 docking models were generated for each tau filament with [^{18}F]PI-2620. The best 10,000 models by the *interface_delta_X* score were clustered based on their pairwise rmsd without superimposition using an average linkage hierarchical clustering algorithm with a cluster cutoff of 8 Å.

MD Simulations. All-atom MD simulations of [^{18}F]PI-2620 with tau filaments were performed at 300 K with Amber 20 using the ff19SB force field for proteins[49] and the general Amber force field[50] for ligand atoms. The tau-[^{18}F]PI-2620 complex was surrounded by an octahedral optimal point charge water box with a thickness of at least 14 Å between any protein or tracer atom and the edge of the box. The charge of the system was neutralized by adding Cl^- ions. SHAKE[51] bond length constraints were applied to all bonds involving hydrogen atoms. Nonbonded interactions were evaluated with a 10 Å cutoff, and electrostatic interactions were calculated by the particle-mesh Ewald method.[52]

The energy of each MD system was first minimized using a three-step minimization procedure: 5000 step minimization of water and ions, 5000 step minimization of protein, and 10,000 step minimization of the whole system. With protein and ligand atoms constrained to their minimized coordinates, the system was then heated from 0 to 300 K over 500 ps in the NVT ensemble with a step size of 1 fs. An Andersen thermostat with a heat-bath coupling time constant of 1 ps was used in this step. After changing to the NPT ensemble, the system was equilibrated at 300 K and a reference pressure of 1 bar for 5 ns with weak positional restraints (with a force constant of 1 kcal mol^{-1} Å^{-2}) applied to the protein backbone and ligand heteroatoms. Langevin dynamics with a collision frequency of 2 ps^{-1} and an integration time step size of 2 fs were used in this step. Positional restraints on protein and ligand atoms were then removed, and the system was equilibrated for another 5 ns without Cartesian restraints.

Production MD was conducted for >500 ns using constant-pressure periodic boundary conditions and Langevin dynamics. Hydrogen mass repartitioning[53] was applied to all non-water hydrogen atoms which allowed using an increased integration time step of 4 fs. Two to four independent MD simulations were carried out for each docking pose and tau filament-[^{18}F]PI-2620 system.

MM/GBSA Energy Calculations. The binding energy ($\Delta G_{binding}$) of [^{18}F]PI-2620 interacting with tau filaments and the per-residue contributions to $\Delta G_{binding}$ were computed in the MM/GBSA procedure[54] with the help of the *MMPBSA.py* program.[55] Starting from the heated and equilibrated MD system, two to four 20 ns-long simulations were conducted for each docking model and filament-[^{18}F]PI-2620 system using an integration time step of 2 fs, constant-pressure periodic boundary conditions, and Langevin dynamics. Molecular conformations were sampled at 50 ps intervals from the last 15 ns of each MD simulation to compute the molecular mechanics energy and solvation free energies. The single trajectory mode was applied, that is, snapshots of the protein, ligand, and protein−ligand complex were taken from the same trajectory. The ionic strength of water was set at 150 mM. The entropic contribution to $\Delta G_{binding}$ was estimated by applying the quasi-harmonic approximation,[56] and ~12,000 conformations of the tau-[^{18}F]PI-2620 complex were used for this analysis.

Metadynamics Simulations. Well-tempered metadynamics simulations of the tau-[^{18}F]PI-2620 system with eight parallel walkers were conducted using GROMACS/2021 with Plumed 2.7.1 plugin.[57−59] The location of the [^{18}F]PI-2620 molecule relative to the filament was described by three spherical coordinates which were used as collective variables in the metadynamics simulation. The definition of these collective variables is depicted in Figure S4. r is the distance between the center of mass of [^{18}F]PI-2620 and that of the filament. θ is the polar angle between the filament−tracer connection vector and the z-axis of the coordinate frame centered on the filament. φ is the azimuthal angle between the x-axis of the filament coordinate frame and the projection of the filament−tracer connection vector onto the x−y plane. An upper-wall repulsive potential was added to limit the sampling of regions that are too far away from the filament and focus on regions surrounding the filament structure. The restraint energy was zero below a distance of ca. 5 Å from the filament surface and grew quadratically beyond that distance with a force constant of 0.5 kcal mol^{-1} Å^{-2}. Gaussian biasing potentials were added every 1 ps with the sigma of the potential being 0.1 Å for r, 0.2 rad for θ, and 0.4 rad for φ. The bias factor was 10, and the initial Gaussian height was 0.287 kcal mol^{-1}. To keep the reference frame fixed, which defines the three collective variables, the system was realigned every step to the backbone atom coordinates of the equilibrated tau-tracer system. Two to three separate 1.6 μs-long metadynamics simulations with different starting positions of [^{18}F]PI-2620 were performed for each tau-[^{18}F]PI-2620 system. The resulting free energy data sets of the individual simulations were averaged to obtain the final free energy map. Convergence of the simulations was checked by performing block analysis and monitoring the time evolution of the free energy. Reweighting of the simulations was done with the driver tool in Plumed and using the method by Parrinello et al.[60]

Brownian Dynamics Simulations. BD simulations of [^{18}F]PI-2620 with tau filaments were performed using the SDA program (version 7).[61,62] For each tau-[^{18}F]PI-2620 system, 10^6 BD trajectories were started from a spherical shell with a radius of 100 Å from the center of the filament. The probability of arriving at the encounter surface at a distance of 6.5 Å from a particular [^{18}F]PI-2620 binding site before the tracer diffused to distances larger than 300 Å from the filament center was calculated. In the BD simulations, the protein and ligand are treated as rigid structures that undergo translational and rotational diffusion in an implicit continuum model. Electrostatic interactions between the tau filament and [^{18}F]PI-2620 were modeled as interactions between an electrostatic potential field derived by solving the Poisson−Boltzmann equation using APBS software[63] for either the protein or ligand and assigning "effective charges" to the other binding partner. The dielectric constant of protein and water was ε = 2.0 and ε = 78.0, respectively, the temperature was 300 K, and the concentration of positive and negative ions was 100 mM. Repulsive interactions were modeled by a volume exclusion term to prevent steric overlap of protein and ligand atoms. Electrostatic desolvation forces and nonpolar interaction forces were modeled by calculating electrostatic desolvation and hydrophobic desolvation potential grids. The average association rate and standard deviation were calculated by bootstrapping with 100 resamples.

■ ASSOCIATED CONTENT

Supporting Information

The Supporting Information is available free of charge at https://pubs.acs.org/doi/10.1021/acschemneuro.2c00291.

All [^{18}F]PI-2620 binding sites in AD-, CBD-, and PSP-tau filaments determined by ligand docking, MM/GBSA energies and interacting residues for all [^{18}F]PI-2620 binding sites determined by ligand docking, setup of the metadynamics simulation, locations of non-proteinaceous EM densities and [^{18}F]PI-2620 docking positions in tau filaments from AD, CBD, and PSP, and PDB structure

https://doi.org/10.1021/acschemneuro.2c00291
ACS Chem. Neurosci. 2022, 13, 2222−2234

files of the most stable [^{18}F]PI-2620 binding complexes (PDF)

AUTHOR INFORMATION

Corresponding Authors

Georg Künze − *Institute for Drug Discovery, University of Leipzig, 04103 Leipzig, Germany;* orcid.org/0000-0003-1799-346X; Email: georg.kuenze@uni-leipzig.de

Osama Sabri − *Department of Nuclear Medicine, University of Leipzig, Leipzig 04103, Germany*; Email: Osama.Sabri@medizin.uni-leipzig.de

Authors

Richy Kümpfel − *Institute for Drug Discovery, University of Leipzig, 04103 Leipzig, Germany*

Michael Rullmann − *Department of Nuclear Medicine, University of Leipzig, Leipzig 04103, Germany*

Henryk Barthel − *Department of Nuclear Medicine, University of Leipzig, Leipzig 04103, Germany*

Matthias Brendel − *Department of Nuclear Medicine, University Hospital of Munich, LMU Munich, 81377 Munich, Germany; German Center for Neurodegenerative Diseases (DZNE), Munich 81377, Germany; Munich Cluster for Systems Neurology (SyNergy), Munich 81377, Germany*

Marianne Patt − *Department of Nuclear Medicine, University of Leipzig, Leipzig 04103, Germany*

Complete contact information is available at: https://pubs.acs.org/10.1021/acschemneuro.2c00291

Author Contributions

G.K., H.B., M.R., and O.S. designed the research and supervised the work. G.K. and R.K. performed the research and analyzed the data. G.K. wrote the initial draft of the manuscript, which was reviewed by all authors. All authors contributed to the interpretation of the data and the revision of the manuscript.

Notes

The authors declare the following competing financial interest(s): H.B. received speaker honoraria from AAA/Novartis, and reader honoraria from LMI. O.S. and M.P. received a research grant from LMI. M.B. received speaker honoraria from Roche, GE healthcare and LMI and is an advisor of LMI. The other authors have no conflicts to disclose.

ACKNOWLEDGMENTS

We thank the Center for Scientific Computing of Leipzig University for providing the computational resources. Funding: M.B. was funded by the Deutsche Forschungsgemeinschaft (DFG) under Germany's Excellence Strategy within the framework of the Munich Cluster for Systems Neurology (EXC 2145 SyNergy—ID 390857198).

REFERENCES

(1) The Alzheimer's Association. Alzheimer's disease facts and figures. *Alzheimer's Dementia* **2021**, *17*, 327−406.

(2) Götz, J.; Halliday, G.; Nisbet, R. M. Molecular Pathogenesis of the Tauopathies. *Annu. Rev. Pathol.: Mech. Dis.* **2019**, *14*, 239−261.

(3) Ganguly, J.; Jog, M. Tauopathy and Movement Disorders—Unveiling the Chameleons and Mimics. *Front. Neurol.* **2020**, *11*, 599384.

(4) Lee, G.; Leugers, C. J. Tau and Tauopathies. *Progress in Molecular Biology and Translational Science*; Teplow, D. B., Ed.; Academic Press, 2012; Vol. *107*, pp 263−293. Available from: https://www.sciencedirect.com/science/article/pii/B9780123858832000047.

(5) Stamelou, M.; Respondek, G.; Giagkou, N.; Whitwell, J. L.; Kovacs, G. G.; Höglinger, G. U. Evolving concepts in progressive supranuclear palsy and other 4-repeat tauopathies. *Nat. Rev. Neurol.* **2021**, *17*, 601−620.

(6) Barbier, P.; Zejneli, O.; Martinho, M.; Lasorsa, A.; Belle, V.; Smet-Nocca, C.; et al. Role of Tau as a Microtubule-Associated Protein: Structural and Functional Aspects. *Front. Aging Neurosci.* **2019**, *11*, 204.

(7) Yang, Y.; Wang, J.-Z. Nature of Tau-Associated Neurodegeneration and the Molecular Mechanisms. *J. Alzheimer's Dis.* **2018**, *62*, 1305−1317.

(8) Wisniewski, H. M.; Merz, P. A.; Iqbal, K. Ultrastructure of Paired Helical Filaments of Alzheimer's Neurofibrillary Tangle. *J. Neuropathol. Exp. Neurol.* **1984**, *43*, 643−656.

(9) Goedert, M.; Spillantini, M. G.; Jakes, R.; Rutherford, D.; Crowther, R. A. Multiple isoforms of human microtubule-associated protein tau: sequences and localization in neurofibrillary tangles of Alzheimer's disease. *Neuron* **1989**, *3*, 519−526.

(10) Goedert, M.; Jakes, R. Expression of separate isoforms of human tau protein: correlation with the tau pattern in brain and effects on tubulin polymerization. *EMBO J.* **1990**, *9*, 4225−4230.

(11) Kovacs, G. G. Invited review: Neuropathology of tauopathies: principles and practice. *Neuropathol. Appl. Neurobiol.* **2015**, *41*, 3−23.

(12) Fitzpatrick, A. W. P.; Falcon, B.; He, S.; Murzin, A. G.; Murshudov, G.; Garringer, H. J.; et al. Cryo-EM structures of tau filaments from Alzheimer's disease. *Nature* **2017**, *547*, 185−190.

(13) Falcon, B.; Zhang, W.; Schweighauser, M.; Murzin, A. G.; Vidal, R.; Garringer, H. J.; et al. Tau filaments from multiple cases of sporadic and inherited Alzheimer's disease adopt a common fold. *Acta Neuropathol.* **2018**, *136*, 699−708.

(14) Falcon, B.; Zhang, W.; Murzin, A. G.; Murshudov, G.; Garringer, H. J.; Vidal, R.; et al. Structures of filaments from Pick's disease reveal a novel tau protein fold. *Nature* **2018**, *561*, 137−140.

(15) Falcon, B.; Zivanov, J.; Zhang, W.; Murzin, A. G.; Garringer, H. J.; Vidal, R.; et al. Novel tau filament fold in chronic traumatic encephalopathy encloses hydrophobic molecules. *Nature* **2019**, *568*, 420−423.

(16) Zhang, W.; Tarutani, A.; Newell, K. L.; Murzin, A. G.; Matsubara, T.; Falcon, B.; et al. Novel tau filament fold in corticobasal degeneration. *Nature* **2020**, *580*, 283−287.

(17) Shi, Y.; Zhang, W.; Yang, Y.; Murzin, A. G.; Falcon, B.; Kotecha, A.; et al. Structure-based classification of tauopathies. *Nature* **2021**, *598*, 359−363.

(18) Dani, M.; Brooks, D. J.; Edison, P. Tau imaging in neurodegenerative diseases. *Eur. J. Nucl. Med. Mol. Imag.* **2016**, *43*, 1139−1150.

(19) Saint-Aubert, L.; Lemoine, L.; Chiotis, K.; Leuzy, A.; Rodriguez-Vieitez, E.; Nordberg, A. Tau PET imaging: present and future directions. *Mol. Neurodegener.* **2017**, *12*, 19.

(20) Lois, C.; Gonzalez, I.; Johnson, K. A.; Price, J. C. PET imaging of tau protein targets: a methodology perspective. *Brain Imaging Behav.* **2019**, *13*, 333−344.

(21) Barthel, H. First Tau PET Tracer Approved: Toward Accurate In Vivo Diagnosis of Alzheimer Disease. *J. Nucl. Med.* **2020**, *61*, 1409−1410.

(22) Wood, H. [11C]PBB3-a new PET ligand that identifies tau pathology in the brains of patients with AD. *Nat. Rev. Neurol.* **2013**, *9*, 599.

(23) Harada, R.; Okamura, N.; Furumoto, S.; Furukawa, K.; Ishiki, A.; Tomita, N.; et al. 18F-THK5351: A Novel PET Radiotracer for Imaging Neurofibrillary Pathology in Alzheimer Disease. *J. Nucl. Med.* **2016**, *57*, 208−214.

(24) Chien, D. T.; Bahri, S.; Szardenings, A. K.; Walsh, J. C.; Mu, F.; Su, M.-Y.; et al. Early Clinical PET Imaging Results with the Novel PHF-Tau Radioligand [F-18]-T807. *J. Alzheim. Dis.* **2013**, *34*, 457−468.

(25) Vermeiren, C.; Motte, P.; Viot, D.; Mairet-Coello, G.; Courade, J. P.; Citron, M.; et al. The tau positron-emission tomography tracer AV-1451 binds with similar affinities to tau fibrils and monoamine oxidases. *Mov. Disord.* **2018**, *33*, 273−281.

(26) Kroth, H.; Oden, F.; Molette, J.; Schieferstein, H.; Capotosti, F.; Mueller, A.; et al. Discovery and preclinical characterization of [18F]PI-2620, a next-generation tau PET tracer for the assessment of tau pathology in Alzheimer's disease and other tauopathies. *Eur. J. Nucl. Med. Mol. Imag.* **2019**, *46*, 2178−2189.
(27) Mueller, A.; Bullich, S.; Barret, O.; Madonia, J.; Berndt, M.; Papin, C.; et al. Tau PET imaging with 18F-PI-2620 in Patients with Alzheimer Disease and Healthy Controls: A First-in-Humans Study. *J. Nucl. Med.* **2020**, *61*, 911−919.
(28) Brendel, M.; Barthel, H.; van Eimeren, T.; Marek, K.; Beyer, L.; Song, M.; et al. Assessment of 18F-PI-2620 as a Biomarker in Progressive Supranuclear Palsy. *JAMA Neurol.* **2020**, *77*, 1408−1419.
(29) Song, M.; Beyer, L.; Kaiser, L.; Barthel, H.; van Eimeren, T.; Marek, K.; et al. Binding characteristics of [^{18}F]PI-2620 distinguish the clinically predicted tau isoform in different tauopathies by PET. *J. Cereb. Blood Flow Metab. Suppl.* **2021**, *27*, 2957−2972.
(30) Tagai, K.; Ono, M.; Kubota, M.; Kitamura, S.; Takahata, K.; Seki, C.; et al. High-Contrast In Vivo Imaging of Tau Pathologies in Alzheimer's and Non-Alzheimer's Disease Tauopathies. *Neuron* **2021**, *109*, 42−58.
(31) Li, L.; Liu, F.; Li, M.; Lu, J.; Sun, Y.; Liang, X.; et al. Clinical Utility of ^{18} F-APN -1607 Tau PET Imaging in Patients with Progressive Supranuclear Palsy. *Mov. Disord.* **2021**, *36*, 2314−2323.
(32) Murugan, N. A.; Nordberg, A.; Ågren, H. Different Positron Emission Tomography Tau Tracers Bind to Multiple Binding Sites on the Tau Fibril: Insight from Computational Modeling. *ACS Chem. Neurosci.* **2018**, *9*, 1757−1767.
(33) Kuang, G.; Murugan, N. A.; Zhou, Y.; Nordberg, A.; Ågren, H. Computational Insight into the Binding Profile of the Second-Generation PET Tracer PI2620 with Tau Fibrils. *ACS Chem. Neurosci.* **2020**, *11*, 900−908.
(34) Zhou, Y.; Li, J.; Nordberg, A.; Ågren, H. Dissecting the Binding Profile of PET Tracers to Corticobasal Degeneration Tau Fibrils. *ACS Chem. Neurosci.* **2021**, *12*, 3487−3496.
(35) Murugan, N. A.; Nordberg, A.; Ågren, H. Cryptic Sites in Tau Fibrils Explain the Preferential Binding of the AV-1451 PET Tracer toward Alzheimer's Tauopathy. *ACS Chem. Neurosci.* **2021**, *12*, 2437−2447.
(36) Meiler, J.; Baker, D. ROSETTALIGAND: protein-small molecule docking with full side-chain flexibility. *Proteins* **2006**, *65*, 538−548.
(37) Davis, I. W.; Baker, D. RosettaLigand docking with full ligand and receptor flexibility. *J. Mol. Biol.* **2009**, *385*, 381−392.
(38) Shi, Y.; Murzin, A. G.; Falcon, B.; Epstein, A.; Machin, J.; Tempest, P.; et al. Cryo-EM structures of tau filaments from Alzheimer's disease with PET ligand APN-1607. *Acta Neuropathol.* **2021**, *141*, 697−708.
(39) Kroth, H.; Oden, F.; Serra, A. M.; Molette, J.; Mueller, A.; Berndt, M.; et al. Structure-activity relationship around PI-2620 highlights the importance of the nitrogen atom position in the tricyclic core. *Bioorg. Med. Chem.* **2021**, *52*, 116528.
(40) Leman, J. K.; Weitzner, B. D.; Lewis, S. M.; Adolf-Bryfogle, J.; Alam, N.; Alford, R. F.; et al. Macromolecular modeling and design in Rosetta: recent methods and frameworks. *Nat. Methods* **2020**, *17*, 665−680.
(41) Alford, R. F.; Leaver-Fay, A.; Jeliazkov, J. R.; O'Meara, M. J.; DiMaio, F. P.; Park, H.; et al. The Rosetta All-Atom Energy Function for Macromolecular Modeling and Design. *J. Chem. Theory Comput.* **2017**, *13*, 3031−3048.
(42) Hanwell, M. D.; Curtis, D. E.; Lonie, D. C.; Vandermeersch, T.; Zurek, E.; Hutchison, G. R. Avogadro: an advanced semantic chemical editor, visualization, and analysis platform. *J. Cheminf.* **2012**, *4*, 17.
(43) Wang, J.; Wang, W.; Kollman, P. A.; Case, D. A. Automatic atom type and bond type perception in molecular mechanical calculations. *J. Mol. Graph. Model.* **2006**, *25*, 247−260.
(44) Moretti, R.; Bender, B. J.; Allison, B.; Meiler, J. Rosetta and the Design of Ligand Binding Sites. *Methods Mol. Biol.* **2016**, *1414*, 47−62.
(45) Kothiwale, S.; Mendenhall, J. L.; Meiler, J. BCL::Conf: small molecule conformational sampling using a knowledge based rotamer library. *J. Cheminf.* **2015**, *7*, 47.
(46) DeLuca, S.; Khar, K.; Meiler, J. Fully Flexible Docking of Medium Sized Ligand Libraries with RosettaLigand. *PLoS One* **2015**, *10*, No. e0132508.
(47) Fleishman, S. J.; Leaver-Fay, A.; Corn, J. E.; Strauch, E.-M.; Khare, S. D.; Koga, N.; et al. RosettaScripts: A Scripting Language Interface to the Rosetta Macromolecular Modeling Suite. *PLoS One* **2011**, *6*, No. e20161.
(48) Lemmon, G.; Meiler, J. Rosetta Ligand docking with flexible XML protocols. *Methods Mol. Biol.* **2012**, *819*, 143−155.
(49) Tian, C.; Kasavajhala, K.; Belfon, K. A. A.; Raguette, L.; Huang, H.; Migues, A. N.; et al. ff19SB: Amino-Acid-Specific Protein Backbone Parameters Trained against Quantum Mechanics Energy Surfaces in Solution. *J. Chem. Theory Comput.* **2020**, *16*, 528−552.
(50) Wang, J.; Wolf, R. M.; Caldwell, J. W.; Kollman, P. A.; Case, D. A. Development and testing of a general amber force field. *J. Comput. Chem.* **2004**, *25*, 1157−1174.
(51) Ryckaert, J.-P.; Ciccotti, G.; Berendsen, H. J. C. Numerical-Integration of Cartesian Equations of Motion of a System with Constraints - Molecular-Dynamics of N-Alkanes. *J. Comput. Phys.* **1977**, *23*, 327−341.
(52) Darden, T.; York, D.; Pedersen, L. Particle Mesh Ewald - an N Log(N) Method for Ewald Sums in Large Systems. *J. Chem. Phys.* **1993**, *98*, 10089−10092.
(53) Hopkins, C. W.; Le Grand, S.; Walker, R. C.; Roitberg, A. E. Long-Time-Step Molecular Dynamics through Hydrogen Mass Repartitioning. *J. Chem. Theory Comput.* **2015**, *11*, 1864−1874.
(54) Kollman, P. A.; Massova, I.; Reyes, C.; Kuhn, B.; Huo, S.; Chong, L.; et al. Calculating structures and free energies of complex molecules: combining molecular mechanics and continuum models. *Acc. Chem. Res.* **2000**, *33*, 889−897.
(55) Miller, B. R., 3rd; McGee, T. D., Jr.; Swails, J. M.; Homeyer, N.; Gohlke, H.; Roitberg, A. E. MMPBSA.py: An Efficient Program for End-State Free Energy Calculations. *J. Chem. Theory Comput.* **2012**, *8*, 3314−3321.
(56) Karplus, M.; Kushick, J. N. Method for estimating the configurational entropy of macromolecules. *Macromolecules* **1981**, *14*, 325−332.
(57) Berendsen, H. J. C.; van der Spoel, D.; van Drunen, R. GROMACS: A message-passing parallel molecular dynamics implementation. *Comput. Phys. Commun.* **1995**, *91*, 43−56.
(58) Tribello, G. A.; Bonomi, M.; Branduardi, D.; Camilloni, C.; Bussi, G. PLUMED 2: New feathers for an old bird. *Comput. Phys. Commun.* **2014**, *185*, 604−613.
(59) Barducci, A.; Bussi, G.; Parrinello, M. Well-Tempered Metadynamics: A Smoothly Converging and Tunable Free-Energy Method. *Phys. Rev. Lett.* **2008**, *100*, 020603.
(60) Branduardi, D.; Bussi, G.; Parrinello, M. Metadynamics with Adaptive Gaussians. *J. Chem. Theory Comput.* **2012**, *8*, 2247−2254.
(61) Gabdoulline, R. R.; Wade, R. C. Brownian Dynamics Simulation of Protein-Protein Diffusional Encounter. *Methods* **1998**, *14*, 329−341.
(62) Martinez, M.; Bruce, N. J.; Romanowska, J.; Kokh, D. B.; Ozboyaci, M.; Yu, X.; et al. SDA 7: A modular and parallel implementation of the simulation of diffusional association software. *J. Comput. Chem.* **2015**, *36*, 1631−1645.
(63) Baker, N. A.; Sept, D.; Joseph, S.; Holst, M. J.; McCammon, J. A. Electrostatics of nanosystems: Application to microtubules and the ribosome. *Proc. Natl. Acad. Sci. U.S.A.* **2001**, *98*, 10037−10041.

https://doi.org/10.1021/acschemneuro.2c00291
ACS Chem. Neurosci. 2022, 13, 2222−2234